Article

In situ synthesis of a nickel boron oxide/graphdiyne hybrid for enhanced photo/electrocatalytic H$_2$ evolution

Xue-Peng Yin [†], Shu-Wen Luo [†], Shang-Feng Tang, Xiu-Li Lu *, Tong-Bu Lu [#]

MOE International Joint Laboratory of Materials Microstructure, Institute for New Energy Materials and Low Carbon Technologies, School of Material Science & Engineering, Tianjin University of Technology, Tianjin 300384, China

A R T I C L E   I N F O

A B S T R A C T

Developing highly active catalysts for photo/electrocatalytic water splitting is an attractive strategy to produce H$_2$ as a renewable energy source. In this study, a new nickel boron oxide/graphdiyne (NiB$_i$/GDY) hybrid catalyst was prepared by a facile synthetic approach. Benefitting from the strong electron donating ability of graphdiyne, NiB$_i$/GDY showed an optimized electronic structure containing lower valence nickel atoms and demonstrated improved catalytic performance. As expected, NiB$_i$/GDY displayed a high photocatalytic H$_2$ evolution rate of 4.54 mmol g^{-1} h^{-1}, 2.9 and 4.5 times higher than those of NiB$_i$/graphene and NiB$_i$, respectively. NiB$_i$/GDY also displayed outstanding electrocatalytic H$_2$ evolution activity in 1.0 M KOH solution, with a current density of 400 mA/cm^2 at an overpotential of 478.0 mV, which is lower than that of commercial Pt/C (505.3 mV@400 mA/cm^2). This work demonstrates that GDY is an ideal support for the development of highly active catalysts for photo/electrocatalytic H$_2$ evolution.

1. Introduction

Energy shortages and environmental issues have triggered considerable interest in alternative energy storage and conversion systems [1]. Hydrogen is regarded as a potential substitute for traditional fossil fuels, due to its high energy density and green combustion products [2,3]. Photo/electrocatalytic water splitting is a promising way of converting solar and electric energy into chemical fuels [4–7]. During the past few decades, significant efforts have been made to develop highly efficient catalysts for the H$_2$ evolution reaction (HER). Until now, the best HER catalysts have been based on the noble metals, such as platinum [8]. However, the scarcity and high cost of noble metals hamper their large-scale application. Thus, it is extremely attractive to exploit earth-abundant and cost-efficient catalysts for the HER [9]. Considerable efforts have been devoted to developing new, more efficient non-noble-metal-based catalysts, such as transition-metal dichalcogenides [10–12], phosphides [13–16], carbides [17], and borates [18–20]. However, catalysts using non-noble metals alone often suffer from low active surface areas and inefficient diffusion of charge carriers, resulting in unsatisfactory catalytic performances. To improve their catalytic activities, a large number of non-noble-metal-based nanocomposites have been fabricated by integrating them on supports with high electron transfer rates and high surface areas, such as graphene [19,21,22] and

carbon nanotubes [23,24]. Thus, designing non-noble-metal nanocomposite materials as photo/electrocatalysts with high numbers of surface-active sites and superior stabilities is highly desirable.

Graphdiyne (GDY), a new carbon allotrope, has shown great potential for photo/electrocatalytic water splitting due to its unique chemical and electronic structure [25]. Compared to graphene and other traditional carbon materials, GDY is composed of an sp^2- and sp-hybridized carbon network, which affords GDY favorable semiconductor property, superior electrical conductivity, and robust stability. GDY also possesses uniformly dispersed pores and a large specific surface area, providing an enormous number of sites for anchoring metal ions and constructing stable non-noble-metal-based nanocomposites. Therefore, GDY has been proven to be an ideal support for in situ growth of stable nanocatalysts for water splitting. To date, TiO_2/GDY [26], CdS/GDY [27], and g-C_3N_4/GDY [28] hybrids have been fabricated and applied to photocatalytic water splitting, with GDY displaying improved separation and migration of photoinduced charge carriers, leading to enhanced photocatalytic activities. In addition, MoS_2/GDY [29], WS_2/GDY [30], CoNC/GDY [31], FeCH@GDY [32], Ni-Co-P/GDY [33], and CoLDH@GDY [34] hybrids have also been constructed to enhance their electrocatalytic water splitting performances. However, GDY has never been used to construct a nanocomposite that could be applied as a catalyst in both photocatalytic and electrocatalytic water splitting reactions for H_2 evolution.

In this study, we prepared for the first time a strongly coupled nickel boron oxide/graphdiyne (NiB_i/GDY) hybrid through a facile room-temperature chemical route, for use as a highly active HER catalyst for photo/electrocatalytic H_2 evolution. NiB_i/GDY displayed improved H_2 evolution under visible light irradiation in aqueous solutions when using Eosin Y (EY) as a photosensitizer and triethanolamine (TEOA) as a sacrificial reagent, realizing 2.9 and 4.5 times higher H_2 evolution rates than those of NiB_i/graphene and NiB_i, respectively. Furthermore, NiB_i/GDY showed high HER electrocatalytic activity, achieving a current density of 400 mA/cm^2 at an overpotential of 478.0 mV, lower than that of commercial Pt/C (505.3 mV@400 mA/cm^2). The improved catalytic performance can be attributed to the formation of strongly coupled NiB_i/GDY, in which the strongly electron donating GDY optimized the electronic structure of NiB_i with lower valence Ni sites. These results demonstrate that GDY could be a promising support for in situ synthesis of nanocomposites as highly active photo/electrocatalysts.

2. Experimental

2.1. Catalyst preparation

2.1.1. Synthesis of graphdiyne

Graphdiyne (GDY) was synthesized via an acetylenic cross-coupling reaction, as previously reported [25,35].

For the synthesis of GDY powder, 33 mg of hexaethynylbenzene (HEB) was dissolved in pyridine and slowly

added to a three-necked flask containing copper foils immersed in pyridine. The mixture was protected from light and then heated for 72 h at 110 °C under an Ar atmosphere. After completion of the reaction, the GDY was washed with hot DMF, acetone, HCl, NaOH, and water in turn, and then dried at 50 °C under vacuum for 12 h.

For the synthesis of GDY nanowalls, HEB (10 mg) was dissolved in acetone and added slowly to a three-necked flask containing five treated Cu foams immersed in a mixture of acetone, pyridine, and tetramethylethylenediamine (TMEDA) with a volume ratio of 100:5:1. The mixed solution was heated in the dark and under an Ar atmosphere for 12 h at 50 °C. After the reaction, the GDY nanowalls grown on the Cu foams were washed sequentially with heated DMF and acetone, and dried at 50 °C under vacuum for 12 h.

2.1.2. Synthesis of NiB_i/GDY

For NiB_i/GDY used in photocatalytic HER, GDY powder (8 mg) was dispersed into 4 mL of ultrapure water. Then, an aqueous solution of $Ni(NO_3)_2$ (40 mM, 508 µL) was added to the GDY solution with continuous stirring. After 3 min, 100 µL of a sodium borohydride ($NaBH_4$) solution (3 mg/mL) was added for a further 2 min. The obtained NiB_i/GDY was then washed and dried overnight under vacuum.

For NiB_i/GDY used in electrocatalytic HER, a piece of GDY nanowall was immersed in a solution of $Ni(NO_3)_2$ (40 mM, 20 mL) for 40 min. Then, an $NaBH_4$ solution (0.5 M, 4 mL) was added and allowed to react for another 2 h. After the reaction, the NiB_i/GDY was washed with pure water to get rid of extra Ni^{2+} and NiB_i. The NiB_i/GDY sample was obtained after drying in air.

2.1.3. Synthesis of NiB_i/graphene

Graphene (8 mg) was homodispersed in 4 mL of ultrapure water. Subsequently, an aqueous solution of $Ni(NO_3)_2$ (40 mM, 508 µL) was added to the graphene solution under continuous stirring. After reacting for 3 min, 100 µL of $NaBH_4$ solution (3 mg/mL) was added for another 2 min. The NiB_i/graphene was obtained after washing and drying under vacuum overnight.

2.1.4. Synthesis of NiB_i

$NaBH_4$ solution (0.5 M, 4 mL) was added to an aqueous solution of $Ni(NO_3)_2$ (40 mM, 20 mL) under continuous stirring. After reacting for 2 h at room temperature, a black sample was acquired by centrifugation and washed three times each with pure water and ethanol. The NiB_i sample was finally obtained after drying under vacuum overnight.

2.2. Characterization

The surface morphologies of the as-prepared samples were determined by scanning electron microscopy (SEM, Verios 460L Ultrahigh Resolution Scanning Electron Microscope) and energy dispersive X-ray spectrometry (EDS). Transmission electron microscopy (TEM) was performed using a Tecnai G2 Spirit TWIN at an acceleration voltage of 120 kV. The compositions and surface electronic states of the as-prepared samples

were measured using X-ray photoelectron spectroscopy (XPS, ESCA LAB250Xi). Raman spectra were analyzed using a high-resolution laser confocal fiber Raman spectrometer (HORIBA EVOLVTION, HORIBA Jobinyvon, France) with an excitation wavelength of 532 nm. A fluorescence spectropho-tometer (F-7000, Hitachi, Tokyo, Japan) was employed to ob-tain the photoluminescence (PL) spectra. Fluorescence decay spectra were measured on a MiroTime 200 time-resolved con-focal fluorescence instrument.

### 2.3. Photocatalytic H_2 evolution measurements

In a typical experiment, 2 mg of the as-prepared catalyst was dispersed in 5 mL of a 10% (v/v) aqueous solution of TEOA, then 3 mg of EY was added. Before irradiation, the solu-tion was purged with Ar for 30 min to remove air, followed by irradiation with a 300 W Xe lamp equipped with a UV-cutoff filter ($\lambda > 400$ nm). The reactant solution was maintained at 25 °C by a flow of cooling water. The evolved H_2 was detected us-ing a gas chromatograph (GC-2014+ATF, 230C, Shimadzu, Ja-pan) equipped with a thermal conductivity detector (TCD).

2.4. Electrochemical measurements

Electrochemical measurements were performed on a standardized three-electrode system (CHI 760E, CH Instru-ments) with a working electrode, a saturated Ag/AgCl refer-ence electrode, and a carbon rod counter electrode. The as-prepared samples were directly used as the working elec-trode. Linear sweep voltammetry (LSV) measurements were performed in 1.0 M KOH electrolyte at a scan rate of 5.0 mV/s. All potentials were referenced to the reversible hydrogen elec-trode (RHE) from the Ag/AgCl reference electrode as follows: E(RHE) = E(Ag/AgCl) + 0.198 + 0.059 × pH. For comparison, 9.0 mg of Pt/C was dispersed in 2.5 mL water/ethanol (v/v = 4:1) containing 100 μL of a 5 wt% Nafion solution. The mixture was sonicated for 1 h, then 140 μL of the catalyst ink was loaded onto the Cu foam. The NiB$_i$ and NiB$_i$/graphene inks were pre-pared by dispersing 4 mg of the respective catalyst into 970 μL of ethanol/water (v:v = 1:1) containing 30 μL of a 5 wt% Nafion solution and sonicating them for 1 h. Then, 67 μL of the Ni-B$_i$-containing ink or 250 μL of the NiB$_i$/graphene-containing ink was loading onto the Cu foam. All tests were performed without further iR compensation.

3. Results and discussion

The NiB$_i$/GDY hybrid was prepared by a simple chemical synthesis strategy performed at room temperature. For com-parison, pure NiB$_i$ and NiB$_i$ grown on graphene (Ni-B$_i$/graphene) were also prepared following a similar method to prepare NiB$_i$/GDY. To prepare NiB$_i$/GDY, GDY was immersed in a solution containing Ni^{2+} ions, which could interact with the butadiyne linkages (−C≡C−C≡C−) and anchor on to GDY, as illustrated in Scheme 1. After further reaction with NaBH$_4$, the NiB$_i$ nanosheets were grown in situ on the GDY, leading to the formation of the NiB$_i$/GDY hybrid. The surface morphology and
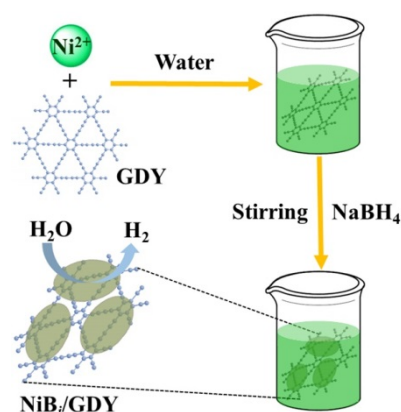
Scheme 1. The in situ growth of NiB$_i$ on GDY at room temperature.

composition of the as-prepared NiB$_i$/GDY were investigated by scanning electron microscopy (SEM), transmission electron microscopy (TEM), and energy dispersive X-ray spectroscopy (EDS). The SEM image of GDY (Fig. 1a) shows a nanosheet ar-ray morphology with an irregular nanowall structure. After NiB$_i$ nanosheets were evenly grown on the surface of GDY, the surface morphology became wrinkled (Fig. 1b), indicating the successful growth of NiB$_i$ on GDY. The TEM images further con-firm the successful construction of the NiB$_i$/GDY hybrid (Fig.e 1c, 1d, and Fig. S1). TEM images were also obtained for Ni-B$_i$/graphene and pure NiB$_i$ (Fig. S2 and Fig. 1e, respectively). NiB$_i$/graphene showed NiB$_i$ nanosheets homogenously orga-nized on the surface of the graphene. Unlike NiB$_i$/GDY and Ni-B$_i$/graphene, pure NiB$_i$ exhibited a hierarchical structure com-prised of aggregated nanosheets (Fig. 1e). In addition, the in-sets of Figs. 1d, 1e, and S2 show the selected area electron dif-fraction (SAED) patterns of NiB$_i$/GDY, NiB$_i$, and NiB$_i$/graphene, respectively, verifying the amorphous structures of the as-prepared samples. Furthermore, the HR-TEM image (Figure S1b) and X-ray powder diffraction (XRD) patterns (Fig. S1c) of NiB$_i$/GDY show no distinct lattice fringes or crystal diffraction peaks, respectively, confirming its amorphous structure [36]. EDS mapping images (Fig. 1f) also reveal uniform distributions of C (green), Ni (red), B (blue), and O (pink) in NiB$_i$/GDY. The above results show that the NiB$_i$/GDY hybrid was successfully
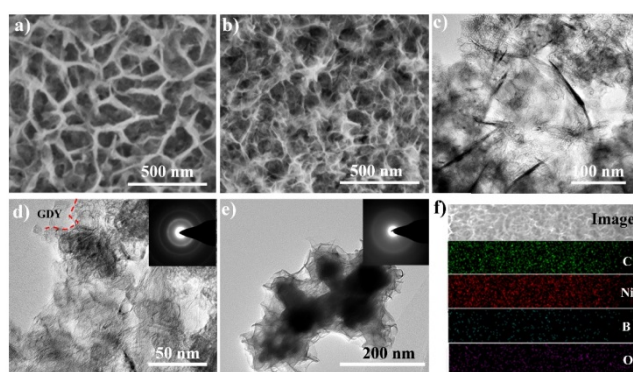

Fig. 1. SEM images of GDY (a) and NiB$_i$/GDY (b); TEM images of Ni-B$_i$/GDY (c, d) and NiB$_i$ (e); the insets of d and e are the corresponding SAED images of NiB$_i$/GDY and NiB$_i$, respectively; (f) EDS mapping im-ages of NiB$_i$/GDY.

synthesized via in situ growth of NiB$_i$ on GDY.

The chemical compositions and electronic structures of samples were evaluated by XRD, Raman spectroscopy, and XPS. As exhibited in Fig. 2a, the XRD pattern of NiB$_i$/GDY demonstrates no distinct diffraction patterns attributable to crystalline nickel compounds, corresponding to the results of the SAED measurements. Figure 2b shows the Raman spectrum of GDY, which contains four distinct peaks at 1394.4, 1544.4, 1923.8, and 2183.3 cm^{-1} in accordance with reported data [25]. Specifically, the peaks at 1394.4 and 1544.4 cm^{-1} are attributed to the D band (the breathing vibration of sp^2 carbons) and G band (the first-order scattering of the E_{2g} mode of the in-phase stretching vibration of sp^2 carbons) of aromatic rings, respectively. Meanwhile, the peaks at 1923.8 and 2183.3 cm^{-1} belong to the typical vibrations of conjugated diyne links ($-C\equiv C\text{-}C\equiv C-$) in GDY. As for NiB$_i$/GDY, the G band peak exhibited an obvious hypsochromic shift to 1580.7 cm^{-1} due to electronic interactions and the electron-donating nature of GDY [28]. In addition, the peaks assigned to $-C\equiv C\text{-}C\equiv C-$ became weaker compared to those of GDY, which could be attributed to the formation of chemical interactions between NiB$_i$ and GDY [37]. As shown in Fig. S3, the survey XPS pattern shows the presence of C, O, B, and Ni in NiB$_i$/GDY, which is consistent with the results of the EDS analysis. The high-resolution C 1s spectrum of NiB$_i$/GDY is shown in Figure S4a. The C 1s peak can be deconvoluted into four subpeaks at 284.42, 285.09, 286.40, and 288.57 eV, which can be assigned to C–C (sp^2), C–C (sp), C–O, and C=O species, respectively [38]. The high-resolution Ni 2p spectra of NiB$_i$ and NiB$_i$/GDY were also compared. As shown in

Figs. S4b and S4c, NiB$_i$ showed two distinct Ni 2$p_{3/2}$ sub-peaks located at 855.9 and 875.5 eV, which could correspond to Ni^{2+} and Ni^{3+}, respectively (as a result of the partial oxidization of the surface). On the other hand, NiB$_i$/GDY exhibited one main Ni 2$p_{3/2}$ peak located at 855.74 eV, which is slightly lower than that seen in NiB$_i$, indicating a lower valence of Ni than Ni^{2+}. This lower valence state demonstrates the strong interaction between NiB$_i$ and GDY, which could optimize the electronic structure and enhance the catalytic performance, as reported in the literature [39–41]. Furthermore, the binding energies of the peaks attributed to Ni 2$p_{3/2}$ and Ni 2$p_{1/2}$ in NiB$_i$ and NiB$_i$/graphene are higher than those seen for NiB$_i$/GDY (Figs. 2c and S5), indicating the presence of Ni ions with lower valence states in NiB$_i$/GDY than those seen in NiB$_i$ and NiB$_i$/graphene. This demonstrates that the strong coupling effect between NiB$_i$ and GDY in the NiB$_i$/GDY hybrid has efficiently tuned the electronic structure of NiB$_i$. In addition, the B 1s spectrum of NiB$_i$/GDY shows a peak at 192.1 eV (Fig. 2d). This can be attributed to B^{3+} from boron oxide species, proving the successful formation of NiB$_i$/GDY.

The photocatalytic H$_2$ evolution performances of NiB$_i$/GDY, NiB$_i$/graphene, NiB$_i$, and GDY were measured in aqueous solutions using TEOA as a sacrificial reagent and EY as a photosensitizer under visible light irradiation (λ > 400 nm). As shown in Fig. 3a, the time courses of the photocatalytic H$_2$ evolution reactions demonstrate that NiB$_i$/GDY showed the best H$_2$ evolution activity. The amount of H$_2$ evolved by NiB$_i$/GDY increased sharply with the time, reaching 31.78 mmol/g after 7 h. This was 2.9 and 4.5 times higher than the performances of Ni-
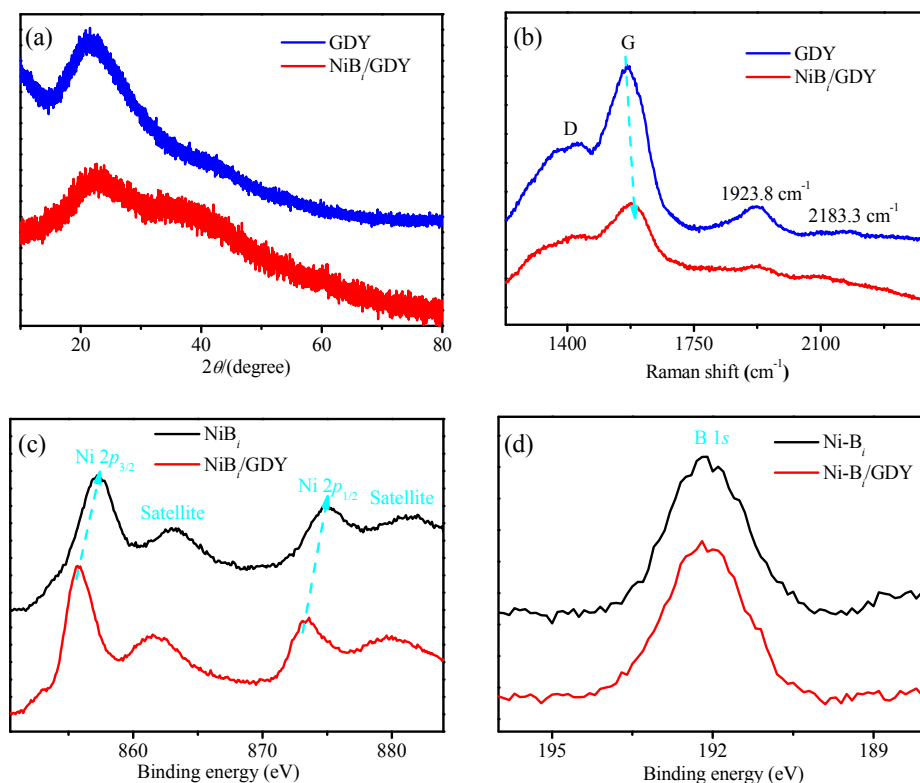
Fig. 2. (a) XRD patterns of GDY and NiB$_i$/GDY, (b) Raman spectra of GDY and NiB$_i$/GDY, (c) Ni 2p, and (d) B 1s XPS patterns of NiB$_i$ and NiB$_i$/GDY.
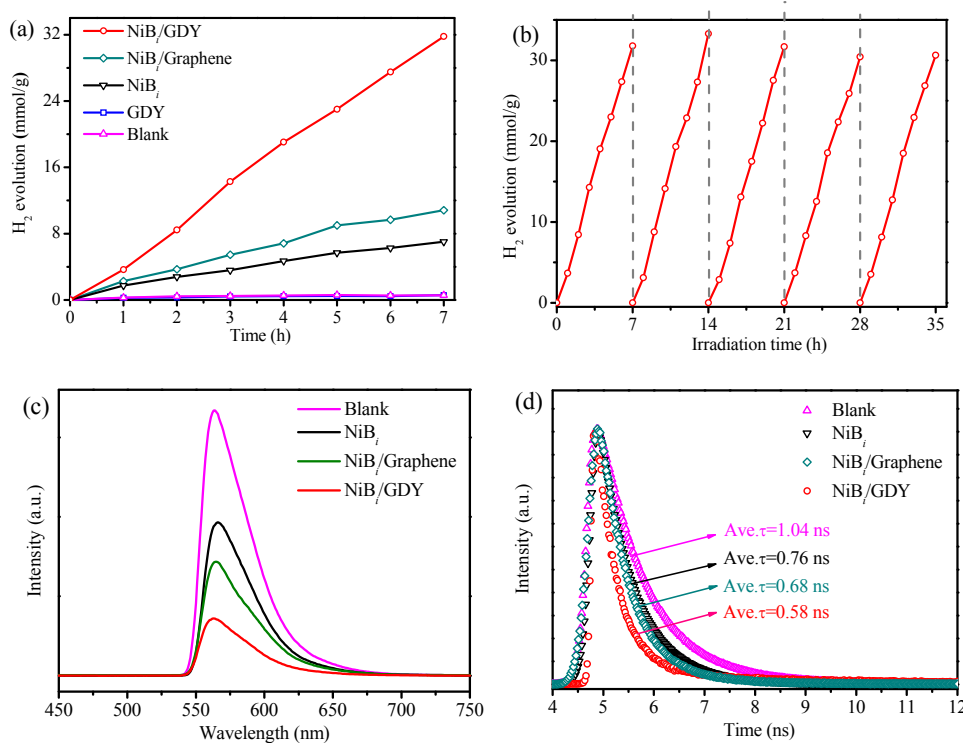
Fig. 3. (a) Time dependence of photocatalytic H_2 generation using NiB_i/GDY, NiB_i/graphene, NiB_i, and GDY catalysts (Reaction conditions: 2 mg catalyst, 3 mg Eosin Y, 5 mL aqueous solution containing 10 vol% TEOA, Xe-lamp (300 W, $\lambda > 400$ nm)). (b) Photocatalytic activity recycling test for Ni-B_i/GDY. (c) Steady-state photoluminescence (PL) spectra of NiB_i/GDY, NiB_i/graphene, and NiB_i. (d) Time-resolved fluorescence decay spectra of Ni-B_i/GDY, NiB_i/graphene, and NiB_i.

B_i/graphene (10.82 mmol/g) and NiB_i (7.02 mmol/g), respectively. The high H_2 evolution activity of NiB_i/GDY can be attributed to its two-dimensional π-conjugated structure, superior electrical conductivity, and the large specific surface area of GDY. The stability of NiB_i/GDY when used for H_2 evolution was also measured by re-dispersing the catalyst in fresh EY/TEOA reaction solutions every 7 h. As shown in Figure S6a and Fig. 3b, NiB_i/GDY maintained its photocatalytic performance, showing no loss in H_2 yield after 5 cycles of 7 h, displaying its excellent stability. Meanwhile, a TEM image of Ni-B_i/GDY after the photocatalytic reaction was also taken (Fig. S6b), confirming the stability of the hybrid during the photocatalytic reaction. In contrast, when using the same ratio of NiB_i to GDY in NiB_i/GDY, the mixture showed poor H_2 reduction activity (Fig. S7). This comparison highlights the importance of the strong coupling effect between GDY and NiB_i in NiB_i/GDY, which optimizes the electronic structure of NiB_i and enhances the photocatalytic HER performance.

The apparent quantum efficiency (AQE) of NiB_i/GDY is shown in Fig. S8. To better comprehend the photocatalytic process, the photoluminescence (PL) and time-resolved fluorescence (TRF) spectra measured. As shown in Fig. 3c, the PL spectrum of an aqueous solution of EY without any catalyst (blank) showed the strongest emission due to severe recombination of photoinduced charge carriers and low H_2 evolution activity. Meanwhile, obvious PL quenching was observed when NiB_i, NiB_i/graphene, or NiB_i/GDY were added to the EY solution, demonstrating that the presence of these materials signif-

icantly promoted the separation of photoinduced charge carriers and that they could act as photocatalysts for H_2 evolution. To further understand the photophysical characteristics of the photoexcited carriers in these systems, the TRF spectra of the samples were measured. As shown in Figure 3d, the average lifetimes obtained from the TRF spectra of blank, NiB_i, Ni-B_i/graphene, and NiB_i/GDY samples were 1.04, 0.76, 0.68, and 0.58 ns, respectively. These results demonstrate that NiB_i/GDY displayed an obvious improvement in the charge carrier separation efficiency in EY solutions when compared to Ni-B_i/graphene and NiB_i, corresponding to the results of the PL measurements. In short, NiB_i/GDY possesses a good ability to promote the separation of photoinduced electrons and holes generated in EY due to the strong coupling effect, resulting in extremely high catalytic activity and stability when used for photocatalytic H_2 evolution.

The electrocatalytic HER activities of NiB_i/GDY, Ni-B_i/graphene, NiB_i, and GDY were also investigated in 1.0 M KOH using a standard three-electrode electrochemical cell. Commercial Pt/C (20 wt%) was used as a reference to accurately evaluate the HER activity. Linear sweep voltammetry (LSV) curves of the different samples were measured at a scan rate of 5 mV/s, as shown in Fig. 4a. As expected, NiB_i/GDY showed enhanced HER activity when compared to GDY, Ni-B_i/graphene, and NiB_i. Notably, NiB_i/GDY achieved a high current density of 400 mA/cm^2 at an overpotential of 478.0 mV, whereas a higher overpotential of 505.3 mV was required to achieve such a current density for the commercial Pt/C catalyst.
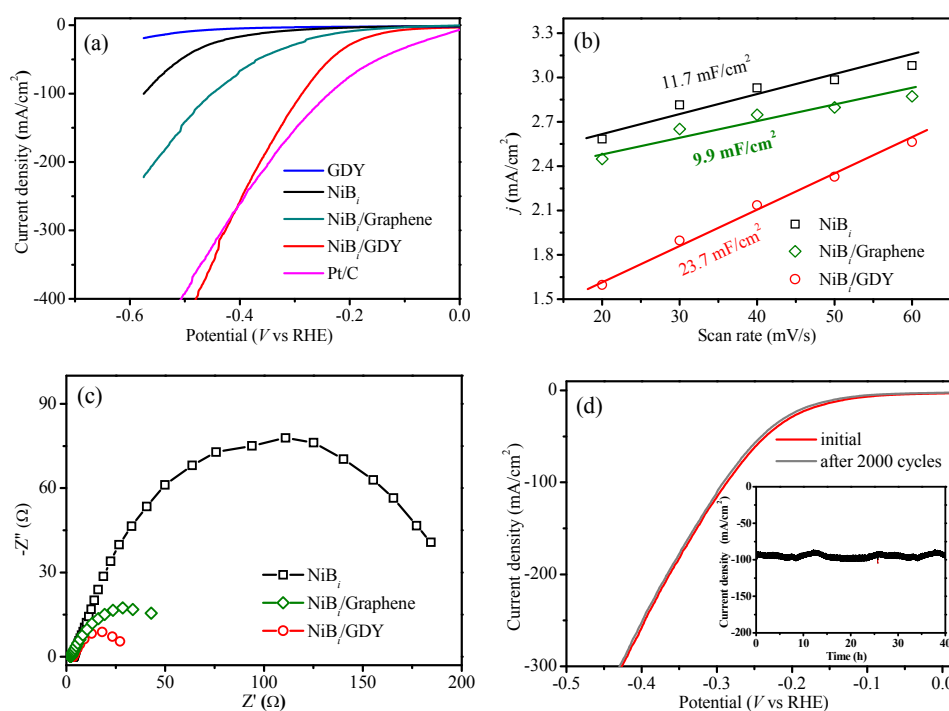
Fig. 4. (a) LSV curves of electrochemical HER activities. (b) Electrochemical surface area (ECSA) measurements of NiB$_i$/GDY, NiB$_i$/graphene, and NiB$_i$ vs. scan rate. (c) Nyquist plots for NiB$_i$, NiB$_i$/graphene, and NiB$_i$/GDY samples at −0.2 V vs. RHE. (d) Polarization curves of NiB$_i$/GDY obtained initially and after 2000 cycles (inset: time dependence of the cathodic current density of NiB$_i$/GDY over 40 h).

In addition, Fig. S9 shows that the Tafel slope of NiB$_i$/GDY was 156.1 mV dec^{-1}, lower than that of NiB$_i$ (298.0 mV dec^{-1}), demonstrating that the Volmer step was rate-determining and that rapid HER kinetics were realized in NiB$_i$/GDY by accelerating the Volmer reaction [42]. The excellent HER performance of NiB$_i$/GDY was possibly due to the strong coupling between NiB$_i$ and GDY, the latter of which significantly improves the conductivity of NiB$_i$/GDY. The electrochemical surface areas of NiB$_i$, NiB$_i$/graphene, and NiB$_i$/GDY were evaluated using their double-layer capacitances (C_{dl}), which were obtained from CV curves measured in the non-Faradic potential range from 0.644–0.744 V at rates varying from 20–60 mV/s in 1.0 M KOH (Figs. 4b and S10). The C_{dl} of NiB$_i$/GDY was calculated to be 23.7 mF/cm^2, much higher than those of NiB$_i$ (11.7 mF/cm^2) and NiB$_i$/graphene (9.9 mF/cm^2), indicating a higher number of exposed active sites after the formation of the NiB$_i$/GDY hybrid. To further understand the kinetic of the HER, Nyquist plots were measured (Fig. 4c), with these showing that the charge transfer resistance of NiB$_i$/GDY was much lower than those of NiB$_i$ and NiB$_i$/graphene. Moreover, both current density-time and long-term CV cycling curves (2000 cycles) confirmed the stability of NiB$_i$/GDY during the HER (Figure 4d).The Ni 2p XPS profiles were also compared to determine the stability of NiB$_i$/GDY during the HER. As shown in Fig. S11, the oxidation states of the catalysts after the electrocatalytic H$_2$ evolution test were similar to those of the as-prepared samples, showing the good stability of NiB$_i$/GDY. These results illustrate that NiB$_i$/GDY possessed excellent activity and stability for the electrocatalytic HER.

4. Conclusions

In summary, we have successfully prepared a new NiB$_i$/GDY hybrid at room temperature via a facile chemical strategy, and investigated its HER catalytic performance for photo/electrocatalytic water splitting. Benefitting from the strong coupling effect between GDY and NiB$_i$, the electron-donating GDY lowered the valence of nickel in NiB$_i$/GDY, resulting in an optimized electronic structure and enhanced photocatalytic HER performance for the NiB$_i$/GDY hybrid. This material showed a H$_2$ evolution rate of 4.54 mmol g^{-1} h^{-1}, which was 2.9 and 4.5 times higher than those of NiB$_i$/graphene and NiB$_i$, respectively, and demonstrated a better electrocatalytic HER performance than commercial Pt/C at high current density. This work not only provides a facile method for the construction of a highly efficient GDY-based catalyst for the HER, but also brings new insights into the development of non-noble-metal catalysts.

Conflict of Interest

The authors declare no conflict of interest.

References

[1] K. Chen, S. Q. Ci, Q. H. Xu, P. W. Cai, M. Z. Li, L. J. Xiang, X. Hu, Z. H. Wen, *Chin. J. Catal.*, **2020**, 41, 858–867.

[2] J. Ran, W. Guo, H. Wang, B. Zhu, J. Yu, S. Z. Qiao, *Adv. Mater.*, **2018**, 30, 1800128.

**Graphical Abstract**

Chin. J. Catal., 2020, 41: 0–0   doi: 10.1016/S1872-2067(20)63601-4

In situ synthesis of a nickel boron oxide/graphdiyne hybrid for enhanced photo/electrocatalytic H$_2$ evolution

Xue-Peng Yin, Shu-Wen Luo, Shang-Feng Tang, Xiu-Li Lu*, Tong-Bu Lu *
Tianjin University of Technology

A new nickel boron oxide/graphdiyne (NiB$_i$/GDY) hybrid was synthesized by a facile room-temperature synthesis approach, which showed outstanding photocatalytic and electrocatalytic H$_2$ evolution activities.
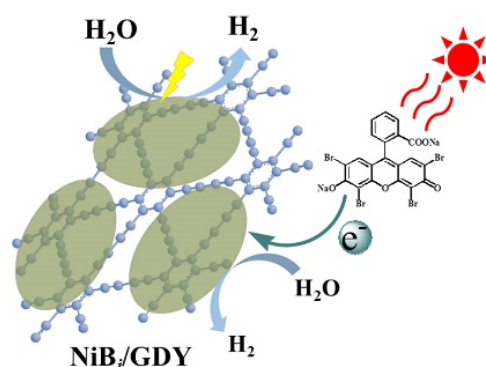
[3] D. D. Li, Y. M. Dong, G. L. Wang, P. P. Jiang, F. Y. Zhang, H. Z. Zhang, J. Li, J. Z. Lyu, Y. Wang, Q. Y. Liu, *Chin. J. Catal.*, **2020**, 41, 889–897.

[4] Q. Liu, J. Tian, W. Cui, P. Jiang, N. Cheng, A. M. Asiri, X. Sun, *Angew. Chem. Int. Ed.*, **2014**, 53, 6710–6714.

[5] Q. Xu, B. Zhu, B. Cheng, J. Yu, M. Zhou, W. Ho, *Appl. Catal. B*, **2019**, 255, 117770.

[6] M. Z. Rahman, K. Davey, S. Z. Qiao, *J. Mater. Chem. A*, **2018**, 6, 1305–1322.

[7] L. Liang, Y. Sun, F. Lei, S. Gao, Y. Xie, *J. Mater. Chem. A*, **2014**, 2, 10647–10653.

[8] Y. Xu, B. Zhang, *Chem. Soc. Rev.*, **2014**, 43, 2439–2450.

[9] C. Guo, X. Liu, L. Gao, X. Ma, M. Zhao, J. Zhou, X. Kuang, W. Deng, X. Sun, Q. Wei, *J. Mater. Chem. A*, **2019**, 7, 21704–21710.

[10] Z. Zhang, W. Li, M. F. Yuen, T. W. Ng, Y. Tang, C. S. Lee, X. Chen, W. Zhang, *Nano Energy*, **2015**, 18, 196–204.

[11] D. Voiry, H. Yamaguchi, J. W. Li, R. Silva, D. C. B. Alves, T. Fujita, M. W. Chen, T. Asefa, V. B. Shenoy, G. Eda, M. Chhowalla, *Nat. Mater.*, **2013**, 12, 850–855.

[12] J. Xie, L. Gao, H. Jiang, X. Zhang, F. Lei, P. Hao, B. Tang, Y. Xie, *Cryst. Growth Des.*, **2019**, 19, 60–65.

[13] C. Huang, Y. Huang, C. Liu, Y. Yu, B. Zhang, *Angew. Chem. Int. Ed.*, **2019**, 58, 12014–12017.

[14] H. Jin, X. Liu, S. Chen, A. Vasileff, L. Li, Y. Jiao, L. Song, Y. Zheng, S. Z. Qiao, *ACS Energy Lett.*, **2019**, 4, 805–810.

[15] B. You, Y. Zhang, Y. Jiao, K. Davey, S. Z. Qiao, *Angew. Chem. Int. Ed.*, **2019**, 58, 11796–11800.

[16] K. Xu, H. Ding, M. Zhang, M. Chen, Z. Hao, L. Zhang, C. Wu, Y. Xie, *Adv. Mater.*, **2017**, 29, 1606980.

[17] H. Lin, Z. Shi, S. He, X. Yu, S. Wang, Q. Gao, Y. Tang, *Chem. Sci.*, **2016**, 7, 3399–3405.

[18] P. Chen, K. Xu, T. Zhou, Y. Tong, J. Wu, H. Cheng, X. Lu, H. Ding, C. Wu, Y. Xie, *Angew. Chem. Int. Ed.*, **2016**, 55, 2488–2492.

[19] M. Q. Yang, J. D. Dan, S. J. Pennycook, X. Lu, H. Zhu, Q. H. Xu, H. J. Fan, G. W. Ho, *Mater. Horiz.*, **2017**, 4, 885–894.

[20] Z. C. Zhuang, Y. Li, Z. L. Li, F. Lv, Z. Q. Lang, K. N. Zhao, L. Zhou, L. Moskaleva, S. J. Guo, L. Q. Mai, *Angew. Chem. Int. Ed.*, **2018**, 57, 496–500.

[21] J. Bao, J. F. Xie, F. C. Lei, Z. L. Wang, W. J. Liu, L. Xu, M. L. Guan, Y. Zhao, H. M. Li, *Catalysts*, **2018**, 8, 350.

[22] J. Bao, X. Zhang, L. Bai, W. Bai, M. Zhou, J. Xie, M. Guan, J. Zhou, Y.

Xie, *J. Mater. Chem. A*, **2014**, 2, 10876–10881.

[23] F. Li, R. Xu, Y. Li, F. Liang, D. Zhang, W. F. Fu, X. J. Lv, *Carbon*, **2019**, 145, 521–528.

[24] L. Najafi, S. Bellani, R. OropesaNuñez, M. Prato, B. Martín García, R. Brescia, F. Bonaccorso, *ACS nano*, **2019**, 13, 3162–3176.

[25] G. Li, Y. Li, H. Liu, Y. Guo, Y. Li, D. Zhu, *Chem. Commun.*, **2010**, 46, 3256–3258.

[26] J. Li, Z. Xie, Y. Xiong, Z. Li, Q. Huang, S. Zhang, J. Zhou, R. Liu, X. Gao, C. Chen, L. Tong, J. Zhang, Z. Liu, *Adv. Mater.*, **2017**, 29, 1700421.

[27] J. X. Lv, Z. M. Zhang, J. Wang, X. L. Lu, W. Zhang, T. B. Lu, *ACS Appl. Mater. Interfaces*, **2019**, 11, 2655–2661.

[28] Y. Y. Han, X. L. Lu, S. F. Tang, X. P. Yin, Z. W. Wei, T. B. Lu, *Adv. Energy Mater.*, **2018**, 8, 1702992.

[29] H. Yu, Y. Xue, L. Hui, C. Zhang, Y. Zhao, Z. Li, Y. Li, *Adv. Funct. Mater.*, **2018**, 28, 1707564.

[30] Y. Yao, Z. Jin, Y. Chen, Z. Gao, J. Yan, H. Liu, J. Wang, Y. Li, S. Liu, *Carbon*, **2018**, 129, 228–235.

[31] Y. Xue, J. Li, Z. Xue, Y. Li, H. Liu, D. Li, W. Yang, Y. Li, *ACS Appl. Mater. Interfaces*, **2016**, 8, 31083–31091.

[32] L. Hui, D. Jia, H. Yu, Y. Xue, Y. Li, *ACS Appl. Mater. Interfaces*, **2019**, 11, 2618–2625.

[33] X. Yin, D. Lu, J. Wang, X. Lu, *ChemCatChem*, **2019**, 11, 5407–5411.

[34] Y. Fang, Y. Xue, L. Hui, H. Yu, Y. Liu, C. Xing, F. Lu, F. He, H. Liu, Y. Li, *Nano Energy*, **2019**, 59, 591–597.

[35] J. Zhou, X. Gao, R. Liu, Z. Xie, J. Yang, S. Zhang, G. Zhang, H. Liu, Y. Li, J. Zhang, Z. Liu, *J. Am. Chem. Soc.*, **2015**, 137, 7596–7599.

[36] Q. Zhu, B. Qiu, M. Du, M. Xing, J. Zhang, *Ind. Eng. Chem. Res.*, **2018**, 57, 8125–8130.

[37] H. Ren, H. Shao, L. Zhang, D. Guo, Q. Jin, R. Yu, L. Wang, Y. Li, Y. Wang, H. Zhao, D. Wang, *Adv. Energy Mater.*, **2015**, 5, 1500296.

[38] X. Gao, J. Li, R. Du, J. Zhou, M. Y. Huang, R. Liu, J. Li, Z. Xie, L. Z. Wu, Z. Liu, J. Zhang, *Adv. Mater.*, **2017**, 29, 1605308.

[39] C. Zhu, A. L. Wang, W. Xiao, D. Chao, X. Zhang, N. H. Tiep, S. Chen, J. Kang, X. Wang, J. Ding, J. Wang, H. Zhang, H. J. Fan, *Adv. Mater.*, **2018**, 30, 1705516.

[40] T. Liu, A. Li, C. Wang, W. Zhou, S. Liu, L. Guo, *Nanoscale*, **2018**, 30, 1803590.

[41] M. Q. Yang, J. Dan, S. J. Pennycook, X. Lu, H. Zhu, Q. H. Xu, H. J. Fan, G. W. Ho, *Mater. Horiz.*, **2017**, 4, 885–894.

[42] L. Diao, B. Zhang, Q. Sun, N. Wang, N. Zhao, C. Shi, E. Liu, C. He,

原位合成氧化镍硼/石墨炔杂化材料用于提高光/电催化产氢性能

殷学鹏[†], 罗舒文[†], 唐上峰, 卢秀利[*], 鲁统部[#]

天津理工大学新能源材料与低碳技术研究院, 材料微结构国际合作联合实验室材料科学与工程学院, 天津300384

摘要: 当今世界面临着严峻的能源紧缺和环境污染问题, 发展高效无污染的清洁能源替代传统化石能源成为近几十年科研工作者的研究热点. 其中, 氢能由于具有燃烧值高、产物无污染等优点成为理想的替代能源. 光/电催化水分解产生氢气是最有效的制氢方法之一. 目前, 高活性的产氢催化剂仍以贵金属为主, 但贵金属高昂的价格和稀缺性等限制了其大规模应用, 因此开发和设计廉价、高效的非贵金属产氢催化剂变得尤为重要. 为了提高非贵金属催化剂的催化活性, 基于非贵金属的复合材料的构建得到广泛研究. 例如, 通过非贵金属和碳材料的复合, 能够提高其比表面积和电子传输速率, 优化活性位点的电子结构, 从而提高催化活性.

石墨炔(GDY)作为一种新兴碳材料, 由sp^2-和sp-杂化碳共同组成. 由于GDY具有高度π共轭结构、大的比表面积和独特的双炔键, 可作为载体与非贵金属离子相互作用形成复合材料, 制备高效产氢催化剂. 基于此, 本工作首次在室温下原位合成了强耦合相互作用的氧化镍硼/石墨炔(NiB$_i$/GDY)催化剂, 并将其应用于光/电催化产氢反应. 在光催化产氢反应中, 采用曙红为光敏剂, 三乙醇胺为牺牲剂, 可见光下NiB$_i$/GDY的光催化产氢速率可达4.54 mmol g^{-1} h^{-1}, 产氢速率分别是氧化镍硼/石墨烯(NiB$_i$/graphene)和NiB$_i$的2.9倍和4.5倍. 此外, NiB$_i$/GDY在1.0 M KOH溶液中也表现出良好电催化产氢性能, 电流密度为400 mA/cm^{2}时其过电位为478.0 mV, 低于商业铂碳(505.3 mV@400 mA/cm^2). NiB$_i$/GDY在光/电催化产氢实验中表现出的优异催化性能可归因于NiB$_i$和GDY之间强耦合相互作用对NiB$_i$电子结构的优化. 上述研究结果表明, GDY可作为理想载体制备高效的光/电催化剂, 同时该工作为设计高效稳定的非贵金属产氢催化剂提供了一定的借鉴意义.

关键词: 石墨炔; 杂化材料; 光电催化剂; 水分解反应; 氢析出

For Author Index:

YIN Xue-Peng, LUO Shu-Wen, TANG Shang-Feng, LU Xiu-Li, LU Tong-Bu

Supporting Information for

In situ synthesis of a nickel boron oxide/graphdiyne hybrid for enhanced photo/electrocatalytic H₂ evolution

Xue-Peng Yin [†], Shu-Wen Luo [†], Shang-Feng Tang, Xiu-Li Lu [*], Tong-Bu Lu [#]

MOE International Joint Laboratory of Materials Microstructure, Institute for New Energy Materials and Low Carbon Technologies, School of Material Science & Engineering, Tianjin University of Technology, Tianjin 300384, China

[*] Corresponding author. Tel/Fax: +86-022-60215704; E-mail: luxiuli@email.tjut.edu.cn
[#] Corresponding author. E-mail: lutongbu@tjut.edu.cn
[†] These authors contributed equally to this work.

The monochromatic light was from different LED lamp (425, 470 and 525 nm). The details of AQE calculation were below,

$$AQE= \frac{2 \times \text{the number of produced H}_2 \text{ molecules}}{\text{the number of incident photons}} \times 100\% = \frac{2 \times M \times N_A \times h \times c}{S \times P \times t \times \lambda} \times 100\%$$

Where M is the molar amount of H₂ molecules, N_A is Avoga-dro constant, h is the Planck constant, c is the speed of light, S is the irradiation area, P is the intensity of the irradiation, t is the photoreaction time and λ is the wavelength of the monochromatic light.
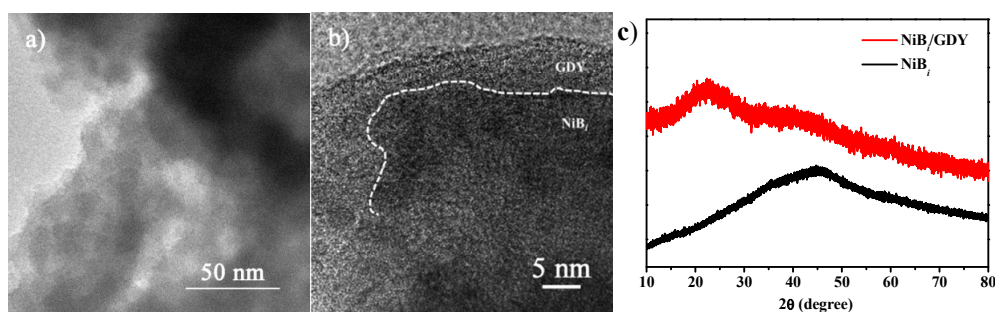

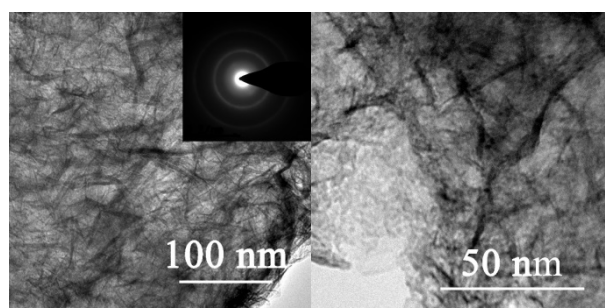**Fig. S1.** (a) TEM image of GDY; (b) HR-TEM image of NiB$_i$/GDY; (c) The XRD patterns for NiB$_i$ and NiB$_i$/GDY.

Fig. S2. TEM images for NiB$_i$/Graphene, the inset is the corresponding SAED image for NiB$_i$/Graphene.
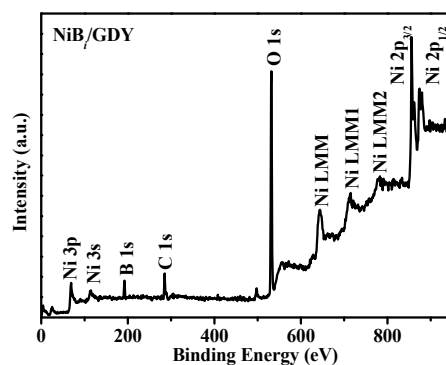

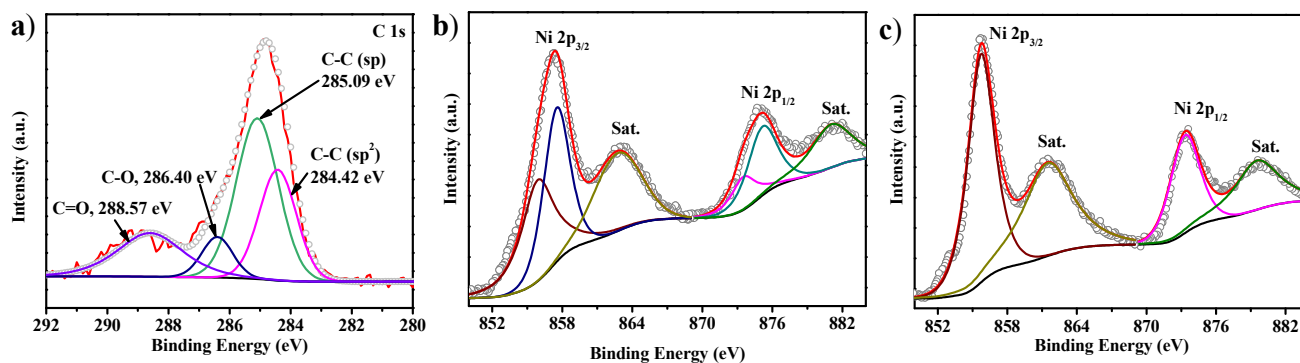**Fig. S3.** XPS survey spectrum for NiB$_i$/GDY.

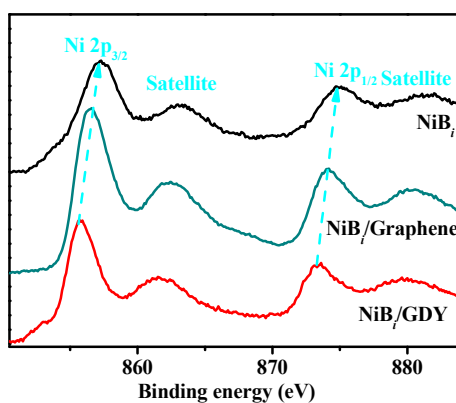**Fig. S4.** High-resolution XPS spectra of C 1s for NiB$_i$/GDY (a); Ni 2p for NiB$_i$ (b) and Ni 2p NiB$_i$/GDY (c).

Fig. S5. XPS patterns of Ni 2p for NiB$_i$, NiB$_i$/Graphene and NiB$_i$/GDY.
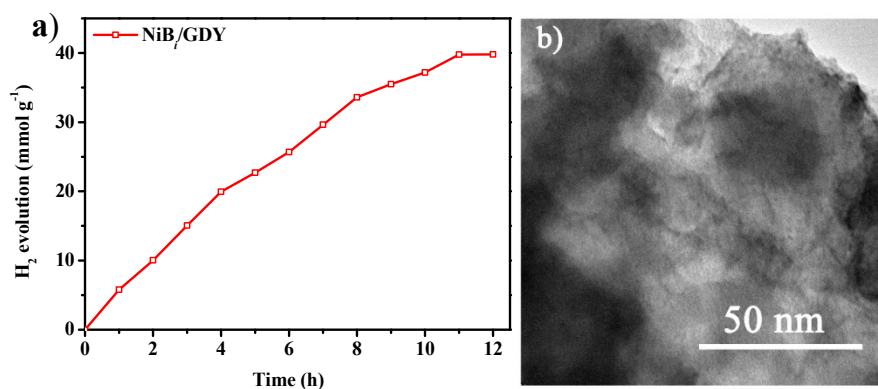

Fig. S6. (a) Long-term photocatalytic H$_2$ generation of NiB$_i$/GDY; (b) The TEM for NiB$_i$/GDY after the photocatalytic reaction.
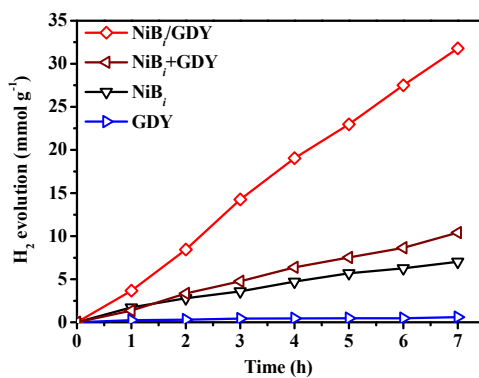

Fig. S7. Time-dependent of photocatalytic H$_2$ generation over the NiB$_i$/GDY, NiB$_i$+GDY, NiB$_i$ and GDY.
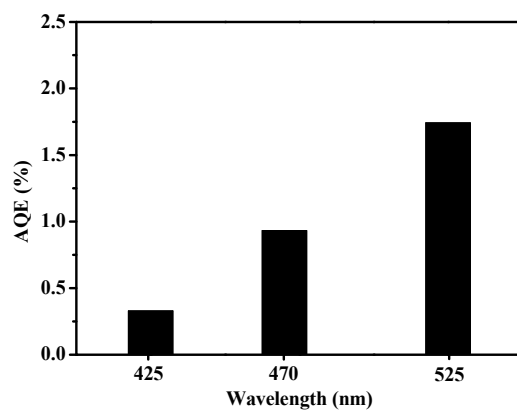
Fig. S8. the Wavelength dependent AQE for NiB$_i$/GDY. Conditions: 2 mg NiB$_i$/GDY, 3 mg Eosin Y (EY), 0.5 mL TEOA and 4.5 mL H$_2$O.

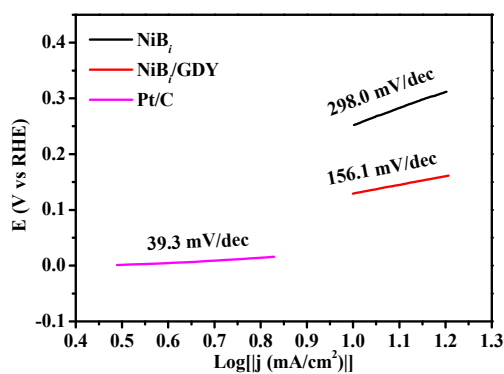
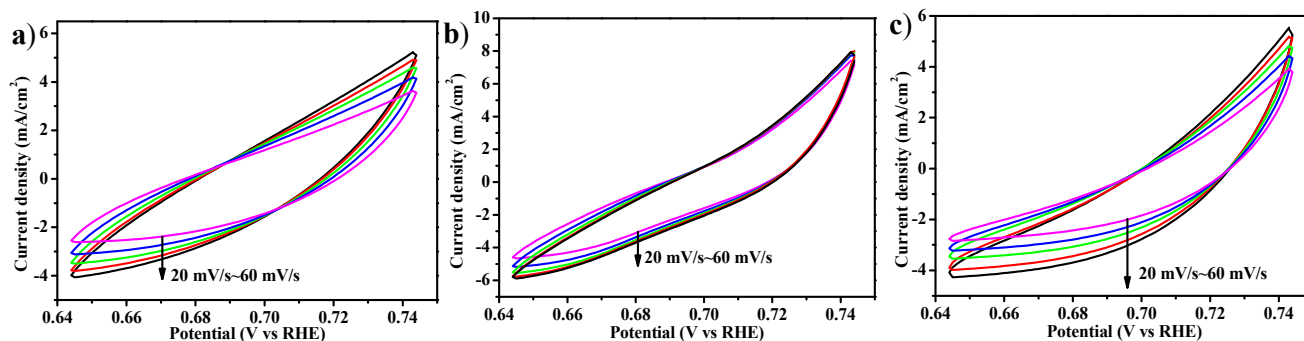**Fig. S9.** Tafel plots for alkaline HER of NiB$_i$, NiB$_i$/GDY and Pt/C.

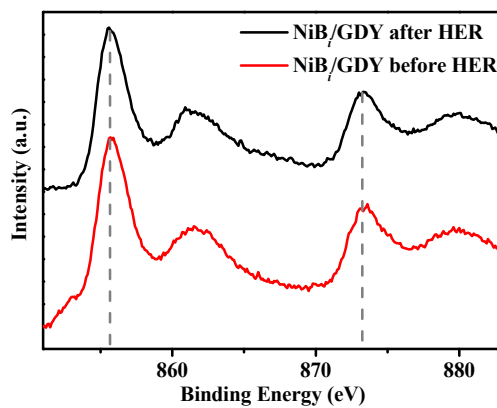**Fig. S10.** Typical CV curves for NiB$_i$ (a), NiB$_i$/Graphene (b) and NiB$_i$/GDY (c).

Fig. S11. XPS patterns for Ni 2p of NiB$_i$/GDY before and after HER.

Table S1
Comparison of the photochemical HER performances of representative nickel-containing photocatalysts.

Catalysts	Light source	Activity (μmol g^{-1} h^{-1})	Source
NiB$_i$/GDY	300 W Xe/400 nm	4540	This work
NiB$_i$/Graphene	300 W Xe/400 nm	1546	This work
Ni$_2$P NS$_S$	300 W Xe/420 nm	2258	[1]
Ni@MOF-5	300 W Xe/420 nm	3022	[2]
NiS/ZnIn$_2$S$_4$	320 W Xe/420 nm	3333	[3]
Ni$_{12}$P$_5$/g-C$_3$N$_4$	300 W Xe/420 nm	536	[4]
Ni$_2$P–sg-CN	300 W Xe/420 nm	330	[5]
NiSCN	300 W Xe/420 nm	2021	[6]
g-C$_3$N$_4$/CB/NiS	300 W Xe	366	[7]
Ni$_2$P/MIL-125-NH$_2$	300 W Xe/420 nm	3878	[8]
15% Ni$_3$C/MAPbI$_3$	300 W Xe/420 nm	2362	[9]
Ni-doped g-C$_3$N$_4$	Xe/Visible light	156	[10]

Table S2
Comparison of the electrochemical HER performances of representative nickel-containing electrocatalysts.

Catalysts	Electrolyte	η_{10}	η_{100}	Source
NiB$_i$/GDY	1 M KOH	129 mV	287 mV	This work
CoP/NiCoP	1 M KOH	133 mV	210 mV	[11]
Ni@NiFe LDH	1 M KOH	92 mV	233 mV	[12]
100-NCT-NiCo$_2$S$_4$	1 M KOH	183 mV	295 mV	[13]
Ni/Mo$_2$C(1:2)-NCNFs	1 M KOH	143 mV	195 mV	[14]
PO-Ni/Ni-N-CNFs-800+300	1 M KOH	262 mV	NA	[15]
Ni(OH)$_2$-Fe$_2$P/TM	0.5 M KOH	196 mV	NA	[16]
Ni NP|Ni-N-C/EG	1 M KOH	147 mV	NA	[17]
P-NiFe	1 M KOH	75 mV	NA	[18]
CoP@C-NPs/GA-5	1 M KOH	225 mV	NA	[19]
Ni-BDT-A	1 M KOH	80 mV	150 mV	[20]
Ni$_{0.9}$Fe$_{0.1}$PS$_3$	1 M KOH	72 mV	NA	[21]
NiΦCFC	1 M KOH	131 mV	NA	[22]
NiCo$_2$S$_4$ NW/GDF	1 M KOH	170 mV//20 mA/cm^2	253 mV	[23]
Co–Ni–P-2	1 M KOH	103 mV	NA	[24]

NA: not provided in the data.

References

[1] S. H. Li, N. Zhang, X. Xie, R. Luque, Y. J. Xu, *Angew. Chem. Int. Ed.*, **2018**, 57, 13082–13085.

[2] W. Zhen, J. Ma, G. Lu, *Appl. Catal. B*, **2016**, 190, 12–25.

[3] A. Yan, X. Shi, F. Huang, M. Fujitsuka, T. Majima, *Appl. Catal. B*, **2019**, 250, 163–170.

[4] D. Zeng, W. J. Ong, H. Zheng, M. Wu, Y. Chen, D. L. Peng, M. Y. Han, *J. Mater. Chem. A*, **2017**, 5, 16171–16178.

[5] A. Indra, A. Acharjya, P. W. Menezes, C. Merschjann, D. Hollmann, M. Schwarze, M. Aktas, A. Friedrich, S. Lochbrunner, A. Thomas, M. Driess, *Angew. Chem. Int. Ed.*, **2017**, 56, 1653–1657.

[6] C. Sun, H. Zhang, H. Liu, X. Zheng, W. Zou, L. Dong, L. Qi, *Appl. Catal. B*, **2018**, 235, 66–74.

[7] J. Wen, J. Xie, Z. Yang, R. Shen, H. Li, X. Luo, X. Chen, X. Li, *ACS Sustain. Chem. & Eng.*, **2017**, 5, 2224–2236.

[8] S. Kampouri, T. N. Nguyen, C. P. Ireland, B. Valizadeh, F. M. Ebrahim, G. Capano, D. Ongari, A. Mace, N. Guijarro, K. Sivula, A. Sienkiewicz, L. Forró, B. Smit, K. C. Stylianou, *J. Mater. Chem. A*, **2018**, 6, 2476–2481.

[9] Z. Zhao, J. Wu, Y. Z. Zheng, N. Li, X. Li, X. Tao, *ACS Catal.*, **2019**, 9, 8144–8152.

[10] P. Deng, J. Xiong, S. Lei, W. Wang, X. Ou, Y. Xu, Y. Xiao, B. Cheng, *J. Mater. Chem. A*, **2019**, 7, 22385–22397.

[11] Y. Lin, K. Sun, S. Liu, X. Chen, Y. Cheng, W. C. Cheong, Z. Chen, L. Zheng, J. Zhang, X. Li, Y. Pan, C. Chen, *Adv. Energy Mater.*, **2019**, 9, 1901213.

[12] Z. Cai, X. Bu, P. Wang, W. Su, R. Wei, J. C. Ho, J. Yang, X. Wang, *J. Mater. Chem. A*, **2019**, 7, 21722–21729.

[13] F. Li, R. Xu, Y. Li, F. Liang, D. Zhang, W. F. Fu, X. J. Lv, *Carbon*, **2019**, 145, 521–528.

[14] M. Li, Y. Zhu, H. Wang, C. Wang, N. Pinna, X. Lu, *Adv. Energy Mater.*, **2019**, 9, 1803185.

[15] Z. Y. Wu, W. B. Ji, B. C. Hu, H. W. Liang, X. X. Xu, Z. L. Yu, B. Y. Li, S. H. Yu, *Nano Energy*, **2018**, 51, 286–293.

[16] X. Zhang, S. Zhu, L. Xia, C. Si, F. Qu, F. Qu, *Chem. Commun.*, **2018**, 54, 1201–1204.

[17] C. Lei, Y. Wang, Y. Hou, P. Liu, J. Yang, T. Zhang, X. Zhuang, M. Chen, B. Yang, L. Lei, C. Yuan, M. Qiu, X. Feng, *Energy Environ. Sci.*, **2019**, 12, 149–156.

[18] F. S. Zhang, J. W. Wang, J. Luo, R. R. Liu, Z. M. Zhang, C. T. He, T. B. Lu, *Chem. Sci.*, **2018**, 9, 1375–1384.

[19] W. Zhao, X. Lu, M. Selvaraj, W. Wei, Z. Jiang, N. Ullah, J. Liu, J. Xie, *Nanoscale*, **2018**, 10, 9698–9706.

[20] C. Hu, Q. Ma, S. F. Hung, Z. N. Chen, D. Ou, B. Ren, H. M. Chen, G. Fu, N. Zheng, *Chem*, **2017**, 3, 122–133.

[21] B. Song, K. Li, Y. Yin, T. Wu, L. Dang, M. Cabán Acevedo, J. Han, T. Gao, X. Wang, Z. Zhang, J. R. Schmidt, P. Xu, S. Jin, *ACS Catal.*, **2017,** 7, 8549–8557.

[22] L. Yang, W. Zhou, J. Jia, T. Xiong, K. Zhou, C. Feng, J. Zhou, Z. Tang, S. Chen, *Carbon*, **2017**, 122, 710–717.

[23] Y. Xue, Z. Zuo, Y. Li, H. Liu, Y. Li, *Small*, **2017**, 13, 1700936.

[24] Y. Pei, Y. Yang, F. Zhang, P. Dong, R. Baines, Y. Ge, H. Chu, P. M. Ajayan, J. Shen, M. Ye, *ACS Appl. Mater. Interfaces*, **2017**, 9, 31887–31896.